



Stochastic characteristics analysis on GNSS observations and real-time ROTI-based stochastic model compensation method in the ionospheric scintillation environment

Sixiang Cheng¹ · Jianhua Cheng¹ · Nan Zang¹ · Zhetao Zhang² · Guojing Zhao¹ · Sicheng Chen¹

Received: 6 June 2023 / Accepted: 5 May 2024 / Published online: 25 May 2024
© The Author(s), under exclusive licence to Springer-Verlag GmbH Germany, part of Springer Nature 2024

Abstract

Ionospheric scintillation interferes with the global navigation satellite system (GNSS) observation precision by random diffractive residuals, leading the elevation-dependent stochastic model to be invalid for precise point positioning (PPP). Hence, we propose a novel GNSS observation-based stochastic model compensation method incorporating the Rate Of Total electron content (ROT) Index (ROTI) with elevation-dependent model without ionospheric scintillation monitoring receiver (ISMR). As the ionospheric activity changes noticeably around sunset, we analyze the afore-sunset and post-sunset observation variances to extract the scintillation impacts on the stochastic characteristics of GNSS observations. Then, the ROTI sensitivity varying with different elevations needs further consideration. We classify the ROT distribution with ROTI and elevation into a stable afore-sunset portion and a real-time post-sunset portion. The difference between two portions is quantified to establish robust factors and further compensates the elevation-dependent stochastic model. Compared with conventional kinematic PPP, the positioning accuracy in east, north and up components improves by 76.2%, 82.2%, and 78.1% during scintillation period in Hong Kong 2015, respectively. Furthermore, the re-convergence is shortened by 34.2% after signal outages.

Keywords PPP · Ionospheric scintillation · ROTI · Stochastic model

Introduction

Due to the standalone-operation, high-accuracy and flexible-deployment, PPP is widely applied to massive GNSS fields, e.g., geoscience research and smart transportation. Ionospheric delay, which is a critical error mainly generated by signal refraction in propagation on GNSS positioning precision, stability, and continuity, should be carefully processed in the sophisticated and active ionosphere (e.g., along the equator). Equatorial plasma bubble (EPB) is the crucial large-scale ionospheric irregularity occurring around the sunset until night. It probably leads by a strong and sophisticated density gradient in the

ionospheric F-layer bottom (Barros et al. 2018). The signal diffraction induced by EPBs makes the random and rapid fluctuations on the signals' phase and amplitude, even lock-loss issue, known as ionospheric scintillation (Kelley 2009; Crane 1997; Morton et al. 2020). Hence, the ionospheric modeling and processing methods for correcting the poor-quality and scintillation-impacted observations have drawn considerable attention. Ionospheric models, e.g., Klobuchar model (Klobuchar 1987), NeQuick model (Di-Giovanni and Radicella 1990), and GIM model (Hernández-Pajares et al. 2009), can eliminate the refractive portion rather than scintillation impacts. Ionospheric parameterization is another strategy mainly processing the refractive portion in the satellite-station line of sight, which intuitively weakens the strength and convergence of positioning model. Ionosphere-free (IF) combination eliminates the first-order refractive portion. None of the above methods can eliminate the scintillation stochastic perturbations on the GNSS observations. Regardless of the scintillation impacts on PPP, the conventional elevation-dependent stochastic model will be biased, even resulting

✉ Nan Zang
zang6050@163.com

¹ College of Intelligent Systems Science and Engineering, Harbin Engineering University, Harbin 150006, China

² School of Earth Sciences and Engineering, Hohai University, Nanjing 211100, China

in positioning errors to several meters at equatorial latitudes (Moreno et al. 2011). Hence, novel stochastic models and data processing methods are proposed to improve the scintillation-impacted positioning.

Aquino et al. (2009) proposed a GNSS stochastic model based on the receiver tracking model with S_4 and σ_φ indices (Conker et al. 2003), which improved the vertical accuracy up to 38% in GPS relative positioning. The receiver tracking stochastic model improved the accuracy of real-time kinematic positioning (88.4 km baseline) and PPP up to 65% (Park et al. 2017) and 75% (in maximum) (Veettil et al. 2020) in scintillation environment, respectively. Luo et al. (2020a) applied the tracking jitter model to assign the appropriate weights for the scintillation-impacted observations, improving the PPP accuracy by 50%. However, the receiver tracking stochastic model requires ISMR, which is always unavailable for most daily applications. Some researches explored the correlation between the observations' stochastic characteristics under scintillation condition and easy-access parameters like ROTI and S_{4c} , obtained from the geodetic and commercial receivers and therewith proposed new mathematical models and quality control methods (Pi et al. 1997; Yang and Liu 2016; Luo et al. 2020b). Weng et al. (2014) tuned the stochastic model considering the relationship between ROTI level and pseudorange noise, reducing the maximum vertical error to about 2.0 m. Luo et al. (2022) further incorporated ROTI with conventional elevation-dependent stochastic model to achieve 28.9% improvement of PPP accuracy. Li et al. (2022) therewith compensated the stochastic model with both ROTI and multipath parameter (MP), improving the vertical accuracy by 93.1%. Moreover, Zhang et al. (2014) proposed a robust iterative Kalman filter to remain PPP performance during scintillations, integrating with the adjusted observation-deviation detection and cycle slip detection. Luo et al. (2019) analyzed the relationship between the cycle slip detection threshold and ROTI, and extracted it by quadratic polynomial fitting for quality control. As the ROTI calculated values are sensitive to observation quality, ROTI sensitivity to scintillation detection varying with different elevations should be investigated.

In this paper, we first exploit pseudorange Helmert variance estimation (HVE) and phase post-residuals' square to investigate the scintillation impacts on observation precision. Then the relationship between ROTI and elevation is extracted by quartic polynomial fitting as a daily stable ROT distribution. Robust factors are formulated for compensating the elevation-dependent stochastic model in kinematic PPP.

The rest of this paper is organized as follows. IF PPP mathematical model is first formulated. Then the theoretical and numeric analysis of scintillation impacts on observations is presented and the stochastic model compensation method based on ROTI is proposed. Consequently, the proposed method is validated with Hong Kong Continuously Operating Reference Stations (HKCORS) data. The research findings and concluding remarks are summarized final.

PPP mathematical model

The raw pseudorange and phase observation equations are as follows (Leick et al. 2015)

$$P_{k,r,j}^s = \rho_{k,r}^s + T_{k,r}^s - \mu_j t_{k,r}^s + dt_{k,r} - dt_k^s + D_{k,r,j} - d_{k,j}^s + \epsilon_{P_{k,r,j}^s} \tag{1a}$$

$$L_{k,r,j}^s = \rho_{k,r}^s + T_{k,r}^s - \mu_j t_{k,r}^s + dt_{k,r} - dt_k^s + B_{k,r,j} - b_{k,j}^s - a_{r,j}^s + \epsilon_{L_{k,r,j}^s} \tag{1b}$$

where subscript k , r and j are the epoch, receiver and frequency, respectively; the superscript s is the satellite. $\rho_{k,r}^s$ denotes the geometry distance between the receiver r and the satellite s . $T_{k,r}^s$ represents the tropospheric delay; $t_{k,r}^s$ is the refractive ionospheric delay at the first frequency. $\mu_j = f_1^2/f_j^2$ is the ionospheric delay cofactor where f_j denotes the j th frequency. $dt_{k,r}$ and dt_k^s are the receiver and satellite clock errors; $D_{k,r,j}$ and $d_{k,j}^s$ are the receiver and satellite code hardware delays; $B_{k,r,j}$ and $b_{k,j}^s$ denote the receiver and satellite phase hardware delays. $\epsilon_{P_{k,r,j}^s}$ and $\epsilon_{L_{k,r,j}^s}$ are the observation noise of pseudorange and phase, absorbing the unmodeled errors, e.g., multipath effects. $a_{r,j}^s$ denotes the ambiguity in meter.

The systematic errors not shown in (1) can be precisely corrected by empirical models and international GNSS service (IGS) products (Kouba and Héroux 2001; Wu et al. 1993). Moreover, the precise satellite orbit, clock, and differential code biases (DCB) products are applied to eliminate dt_k^s and $d_{k,j}^s$, detailed by Li et al. (2019). The receiver clock error absorbs the code hardware delay $D_{k,r,j}$, which can be reparametrized as IF receiver clock error $dt_{k,r,IF} = dt_{k,r} + \mathbf{J} [D_{k,r,i} \ D_{k,r,j}]^T = (dt_{k,r} + D_{k,r,j}) - \mu_j \delta D_i$ with $\mathbf{J} = \begin{bmatrix} f_i^2/(f_i^2 - f_j^2) & -f_j^2/(f_i^2 - f_j^2) \end{bmatrix}$. Here, i, j are the used frequencies of IF combination. Note that the ambiguities and hardware delays are linear dependent. Thus, the float ambiguity parameter can be reparametrized as $\bar{a}_{r,j}^s = a_{r,j}^s + b_{k,j}^s - B_{k,r,j} - d_{k,j}^s + D_{k,r,j}$.

The first-order ionospheric delays led by ionosphere refraction can be eliminated by IF combination. The IF PPP functional model reads (Leick et al. 2015)

$$\mathbf{P}_{IF,k,r} = \mathbf{A}_{k,r} \mathbf{x}_{k,r} + \mathbf{g}_{k,r} T_{k,r}^s + \mathbf{e}_m dt_{k,r,IF} + \epsilon_{P_{IF,k,r}} \tag{2a}$$

$$\mathbf{L}_{IF,k,r} = \mathbf{A}_{k,r} \mathbf{x}_{k,r} + \mathbf{g}_{k,r} T_{k,r}^s + \mathbf{e}_m dt_{k,r,IF} - \bar{\mathbf{a}}_{IF,r} + \epsilon_{L_{IF,k,r}} \tag{2b}$$

where $\mathbf{P}_{IF,k,r} = [P_{IF,k,r}^1 \ \dots \ P_{IF,k,r}^m]^T$ is the IF pseudorange vector of the m tracked satellite with $\mathbf{P}_{IF,k,r}^s = \mathbf{J} \begin{bmatrix} P_{k,r,i}^s & P_{k,r,j}^s \end{bmatrix}^T$. $\mathbf{L}_{IF,k,r}$ shares a same structure as $\mathbf{P}_{IF,k,r}$. $\mathbf{A}_{k,r}$ denotes the design matrix of the coordinate parameter vector $\mathbf{x}_{k,r}$. $T_{k,r}^s$ is the zenith tropospheric delay with the mapping function coefficient vector $\mathbf{g}_{k,r}$. \mathbf{e}_m is an m -column vector with all

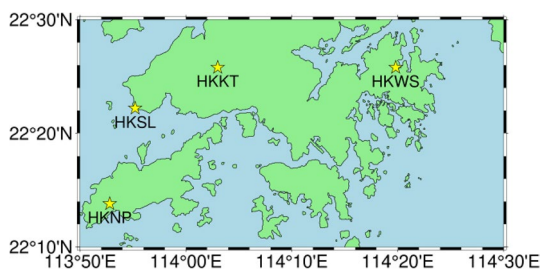


Fig. 1 Geographical locations of HKKT, HKNP, HKSL, and HKWS stations

elements being 1. $\bar{a}_{IF,r} = [a_{IF,k,r}^1 \dots a_{IF,k,r}^m]^T$ is the IF ambiguity vector, where $a_{IF,k,r}^s = J [\bar{a}_{r,i}^s \ \bar{a}_{r,j}^s]^T$.

The PPP stochastic model consists of pseudorange and phase precision as $Q = Q_m \otimes Q_0$ where the symbol \otimes denotes the Kronecker product. $Q_m = \text{diag}(\sigma_p^2, \sigma_L^2)$ captures the precision of pseudorange and phase observations (Zang et al. 2019). Moreover, Q_0 is cofactor matrix describing the elevation-dependent dispersion under Gaussian distribution observation noise. Referring to the error propagation characteristic, IF precision Q_{IF} is amplified as

$$Q_{IF} = \left(f_i^2 / (f_i^2 - f_j^2) \right)^2 Q_i + \left(f_j^2 / (f_i^2 - f_j^2) \right)^2 Q_j \quad (3)$$

where Q_i and Q_j are the stochastic model of the used frequencies, respectively.

Data and ROTI for monitoring ionospheric scintillation

Data source

HKCORS dataset collected from the equatorial ionospheric anomaly region (around 22° 20' N) is adopted for validation. Daily 1 Hz GPS observations from Kam Tin (HKKT), Ngong Ping (HKNP), Siu Lang Shui (HKSL), and Wong Shek (HKWS) stations from day of year (DOY) 274 (October 1st) to 304 (October 31st) in 2015 are collected and shown in Fig. 1. As the high solar flux condition (F10.7 around $127 \times 10^{-22} \text{ Wm}^{-2} \text{ Hz}^{-2}$) is easier to induce the EPB signatures (Barros et al. 2018; Kintner et al. 2009), the span of October 2015 following the peak of 24th solar cycle is more likely to detect the scintillations.

Four stations are equipped with Leica GRX1200 + GNSS receiver and LEIAR25.R4 antenna. Note that HKSL and HKWS changed their receivers on DOY 303 and 299, respectively. To avoid the influence of equipment exchange, HKSL data from DOY 303 to 304 and HKWS data from DOY 300 to 304 are not involved in our experiment. Besides,

the unavailable data from HKWS station during DOY 274 to 279 and HKSL station on DOY 300 are excluded.

ROTI for monitoring ionospheric scintillation

ROT is introduced to reflect the ionospheric activity intensity derived from the epoch-difference dual-frequency phase measurements as (Pi et al. 1997; Liu 2011)

$$ROT_k^s = \frac{f_1^2 f_2^2 (\Delta L_{r,1}^s - \Delta L_{r,2}^s)}{40.3 \times 10^{16} (f_1^2 - f_2^2) \Delta t} \quad (4)$$

where Δ denotes the epoch-difference operation. The ambiguities and receiver hardware delays can be eliminated by epoch difference without any cycle slips (Zhang 2017). Only the ionospheric delay residuals and unmodelled observation noise remain in ROT_k^s . Furthermore, the standard deviation of ROT which is sensitive to the scintillation detection, namely ROTI, is expressed as (Pi et al. 1997)

$$ROTI_k^s = \sqrt{\langle (ROT_k^s)^2 \rangle - \langle ROT_k^s \rangle^2} \quad (5)$$

where $\langle \dots \rangle$ denotes the average operation. To output ROTI continuously, a sliding window with 60 s length is imposed in our work, which is enough to describe the ionospheric activity (Luo et al. 2020b), thus $ROT_k^s = [ROT_k^s \dots ROT_{k-59}^s]^T, k \geq 60$. The unit of ROT is TECU/min, where 1TECU represents 10^{16} electrons/m². Referring to the Ma and Maruyama (2006) study, ROTI (> 0.5TECU/min) can represent the ionospheric irregularities' occurrence with 1/30 Hz dataset. On this basis, following the Jacobsen (2014) study which reveals the strongly positive correlation between ROTI and data sampling rate, ROTI (> 0.5TECU/min) is inferred sensitive enough to find scintillations for 1 Hz data.

Equations (4) and (5) reveal that ROTI is a satellite-specific index reflecting the fluctuation of the ionospheric activity, which should be sensitive to scintillation detection (Yang and Liu 2016). To exclude the interferences of the residual unmodelled errors and cycle slips, the 30° cutoff elevation setting and epoch-wise TurboEdit method (Blewitt 1990) with scintillation-modified thresholds (Zhang et al. 2014) are applied to the ROTI extractions and analysis afterwards. As depicted in Fig. 2, the available ROTI series at HKKT station during local time (LT) 19:00 to 24:00 on DOY 293 reveals that the scintillation-impacted ROTI series significantly exceed 0.5TECU/min and reach 9.60TECU/min in maximum after LT 20:00 (sunset at LT 17:55), which seem to characterize the scintillation process.

Firstly, the scintillation intensity of the experimental dataset is analyzed with ROTI series in both time and magnitude

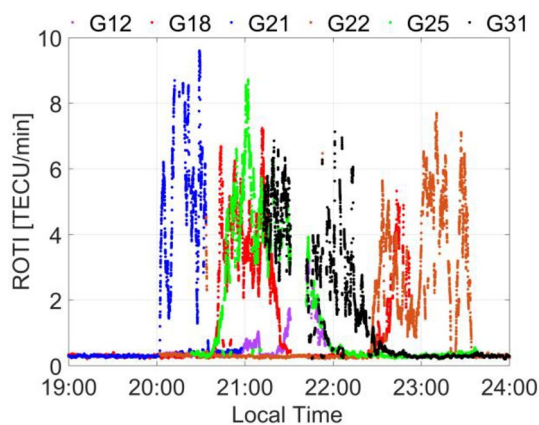


Fig. 2 Available ROTI series (including G12, G18, G21, G22, G25, and G31) at HKKT station on DOY 293

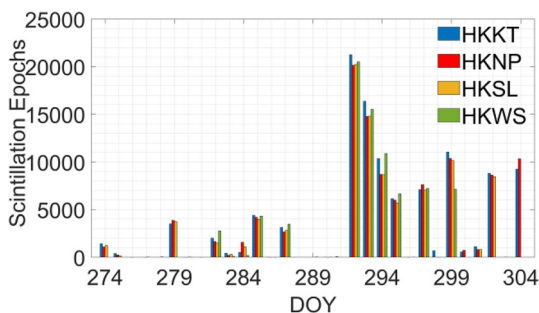
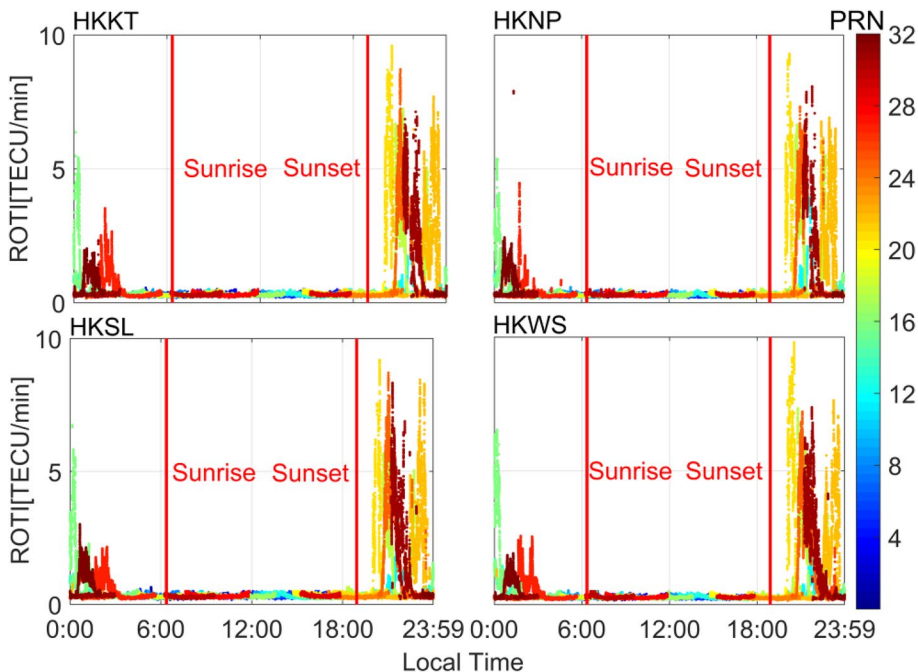


Fig. 3 Daily station-wise scintillation epochs for four stations in October

Fig. 4 Available daily ROTI series on DOY 293 at four stations



scales, preparing for further validations in various scintillation environments. In the time scale, a scintillation epoch is defined for the scintillation duration statistic, as ROTI of at least one satellite exceeds 0.5TECU/min. The scintillation epoch number in October in Fig. 3 shows that different scintillation intensity situations are involved in validation. Even an intensive scintillation process approximating 6 h is available for four stations on DOY 292, with the scintillation epochs exceeding 20,000. The results of scintillation detection are in accordance with the study detected by S_4 and σ_ϕ indices in HK on the same day (Luo et al. 2017, 2020a). Note that extreme low scintillation epoch number shown in Fig. 3 may be generated by the external interferences on the ROTI detection.

To further present the scintillations probably induced by EPBs signatures in the magnitude scale, we extract the available daily ROTI series on LT DOY 293 at four stations in Fig. 4. The EPBs are usually believed to be formed after sunset and persist several hours in extending to the areas of the equatorial ionization anomaly covering the geomagnetic latitudes from about 20°S to 20°N (Ott 1978; Kelley 2009). In every subgraph of Fig. 4, two significant ionospheric active periods during LT 0:00~3:00 and 19:00~24:00 can detect scintillations which are most likely caused by EPBs on DOY 292 and 293, respectively. It further infers that the high ROTI magnitude is one of the EPBs signatures, which describes the scintillation intensity. Moreover, as the EPBs are probably seeded and initiated after sunset, the hourly scintillation epoch percentage are calculated to show the potential occurrence time

of ionospheric scintillations in Fig. 5. The hourly scintillation epoch percentage $SEP_{h,ST}$ of each station is derived as

$$SEP_{h,ST} = \left[\frac{n_{h,ST}}{\sum_{h=0}^{23} n_{h,ST}} \right] \times 100\% \tag{6}$$

where $n_{h,ST}$ denotes the monthly statistic of scintillation epoch at ST station during $h = 0, \dots, 23$ hour in October. As illustrated in Fig. 5, the scintillation epochs are concentrated after sunset. Similar conclusions were given by Luo et al. (2019) and Kelly (2009). Note that a few afore-sunset scintillation epochs caused by external interference like multipath are excluded in further analysis. In conclusion, ROTI is capable to monitor different scintillation intensity in our experiment.

Impact analysis of ionospheric scintillation on observation stochastic characteristics

The ionospheric delay at j th frequency mainly led by the refractive effects in stable ionosphere, whereas both refractive and diffractive portions are induced during scintillations. IF combination can eliminate the first-order refractive portion, which is invalid for the diffractive one. IF residuals during scintillations read

$$\delta i_{k,r,IF}^s = \mathbf{J} \begin{bmatrix} i_{dif,k,r,i}^s & i_{dif,k,r,j}^s \end{bmatrix}^T \tag{7}$$

where $i_{dif,k,r,i}^s$ denotes the diffractive delay at i th frequency. Note that $i_{dif,k,r,i}^s$ and $i_{dif,k,r,j}^s$ may introduce the unmodelled diffractive residuals into IF combinations. Here, considering the random characteristic of the scintillation impacts, we reckon that $i_{k,r,IF}^s$ obeys an epoch-wise zero mean Gaussian distribution with variance depending on scintillation intensity. The random diffractive impacts on the stochastic characteristics of observations in Gaussian distribution are analyzed afterwards. To improve the computation efficiency, an almost unbiased simplified HVE method is applied, reading (Li 2016)

$$\hat{\sigma}_t^2 = \frac{\mathbf{v}_t^T \mathbf{y}_t}{r_t} \tag{8}$$

where $\hat{\sigma}_t^2$ is the variance estimate of the t th observations. \mathbf{v}_t is the residual vector of the t th observations. $r_t = n_t - \text{tr} \left((\mathbf{H}^T \mathbf{P} \mathbf{H})^{-1} \mathbf{H}_t^T \mathbf{P}_t \mathbf{H}_t \right)$ is the redundancy number, where \mathbf{H} denotes the design matrix. Here, n_t and \mathbf{H}_t are the t th observation number and the t th row vector of matrix \mathbf{H} . Note that the phase observation redundancy number of PPP model closes to 0, leading the phase variance $\hat{\sigma}_L^2$ to be inestimable. Thus, only the satellite-specific pseudorange variances are estimated in this paper. The available daily ROTI series on DOY 287 and 293 at HKKT station are depicted in Fig. 6, which include 3126 and 16,361 scintillation-impacted epochs, respectively. The scintillations on DOY 287 and 293 pollute 7 and 10 GPS satellites (ROTI exceeding 0.5TECU/

Fig. 5 Hourly scintillation epoch percentage of four stations in October

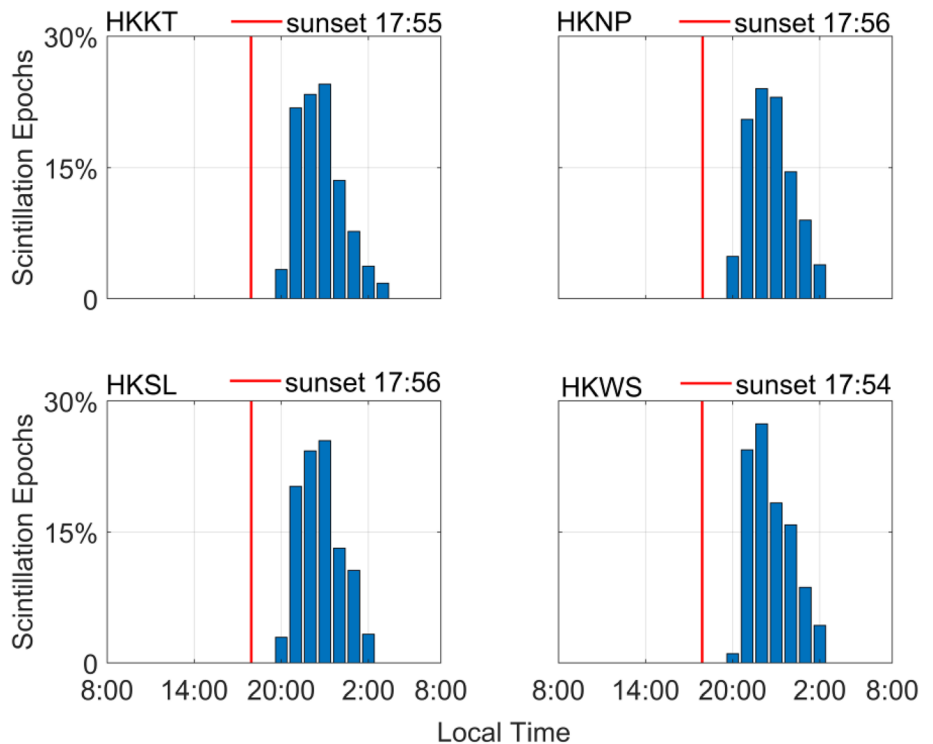


Fig. 6 Available daily ROTI series on DOY 287 (left) and 293 (right) at HKKT station

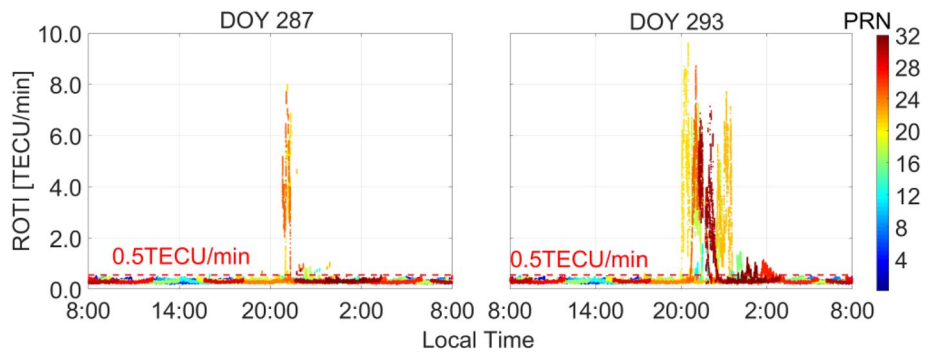


Fig. 7 Post-sunset and afore-sunset HVE results for HKKT station on DOY 287 (left) and 293 (right)

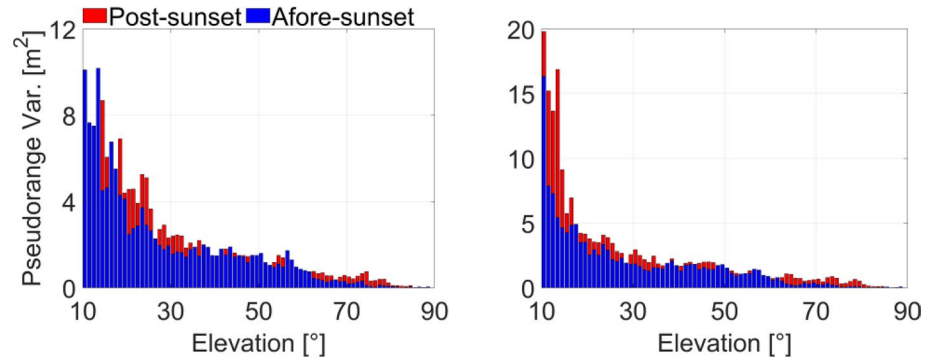
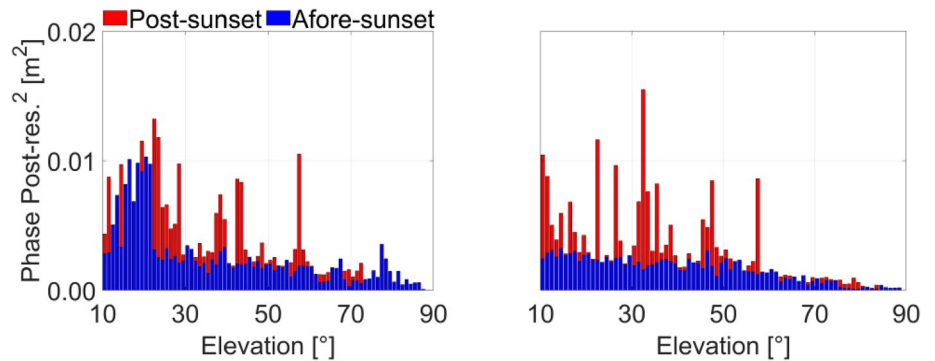


Fig. 8 Post-sunset and afore-sunset square of phase post-residuals for HKKT station on DOY 287 (left) and 293 (right)



min) and the maximum ROTI reaches 8.0TECU/min and 9.6TECU/min, respectively.

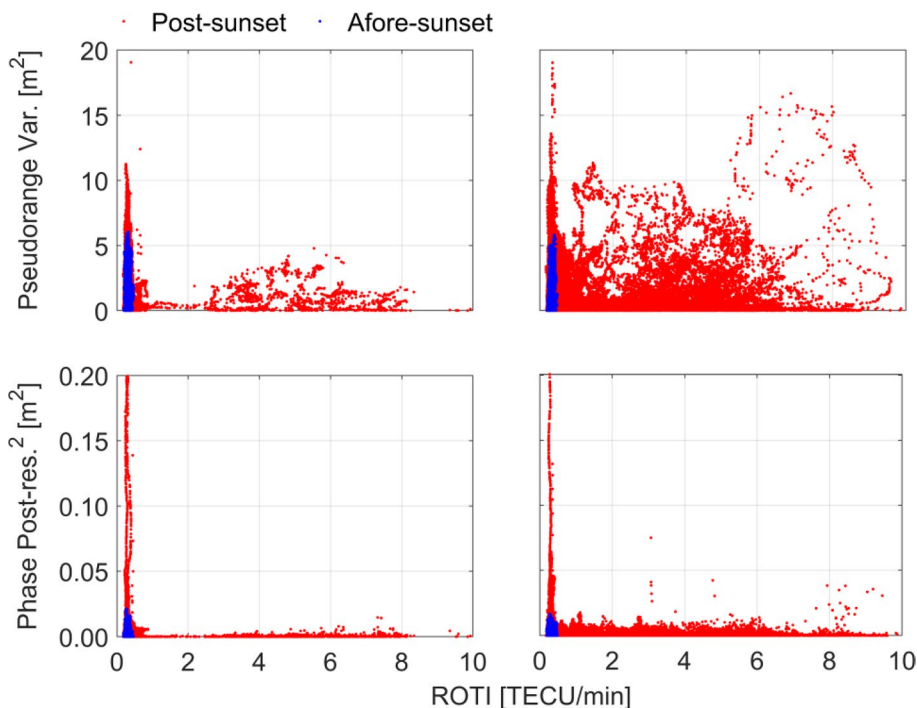
The mean pseudorange HVE values (HKKT station on DOY 287 and 293) for each elevation interval of 1° from 10° to 90° are collected in Fig. 7, where the HVE results are classified into afore-sunset (blue) and post-sunset (red) groups to demonstrate stable and active ionospheric characteristics. The pseudorange precision is overall elevation-dependent before sunset, whereas it is deteriorated by scintillations presented as the red bars. Moreover, the impacts of scintillation on pseudorange precision on DOY 293 are more significant than those on DOY 287, due to the more intense spatiotemporal scintillation happening on DOY 293, shown in Fig. 6.

Furthermore, the post-sunset phase post-residuals indicate that the phase precision are still severely impaired by

scintillations, in Fig. 8. Incorporating with Fig. 7, the differences of precision distribution for phase between the post-sunset and afore-sunset periods is more conspicuous than those for pseudorange, owing to the interferences from the worse observation noise and residual multipath errors.

Figure 9 shows the relationship between ROTI and GNSS observation precision for HKKT station on DOY 287 and 293, classified into post-sunset and afore-sunset periods. There are massive large post-sunset pseudorange variances and square of phase post-residuals with low ROTI (within 0.5TECU/min), impacted by the poor-quality PPP solutions during scintillations. It indicates that the scintillations impair the pseudorange and phase precision more in the intense ROTI environment (post-sunset) than the stable ionosphere environment (afore-sunset).

Fig. 9 Relationship between ROTI and GNSS observation precision including pseudorange variance (*top*) and square of post-residuals (*bottom*) for HKKT station on DOY 287 (*left*) and 293 (*right*), classified into post-sunset (*red*) and afore-sunset (*blue*) periods



The unmodelled diffractive residuals apparently pollute the pseudorange and phase observation precision, leading the empirical elevation-dependent stochastic model to be biased. For lack of redundant observations in variance estimation, the reliability of rigorous HVE model is weakened in real-time PPP. Thus, a reliable stochastic compensation method of the real-time PPP with a simple but adaptive factor describing the scintillation impacts is required for the complex environment. As aforementioned analysis, the phase-based ROTI is applied to design a more robust and adaptive factor for both pseudorange and phase observations.

Real-time ROTI-based stochastic model compensation method

Daily stable ionosphere ROT distribution

To extract the stochastic characteristics of ROT distribution in different environments, we depict the ROT distribution at HKKT station on DOY 291 (scintillation-free) and 293 (13,043 scintillation epochs) in Fig. 10. The ROT distribution on DOY 291 approximately obeys a zero-mean Gaussian distribution with 0.5TECU/min standard deviation (seeing the red line). As ROT is relatively stable over a short period (60 s in this paper), the impacts of the ROT trend term on ROTI can be ignored. Thus, we consider that ROT_k^s follows epoch-wise zero mean Gaussian distribution as follow

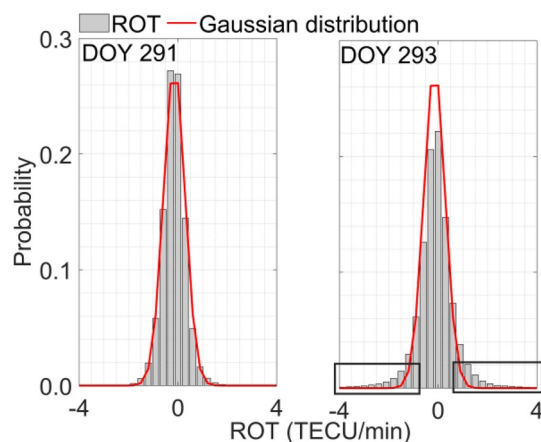
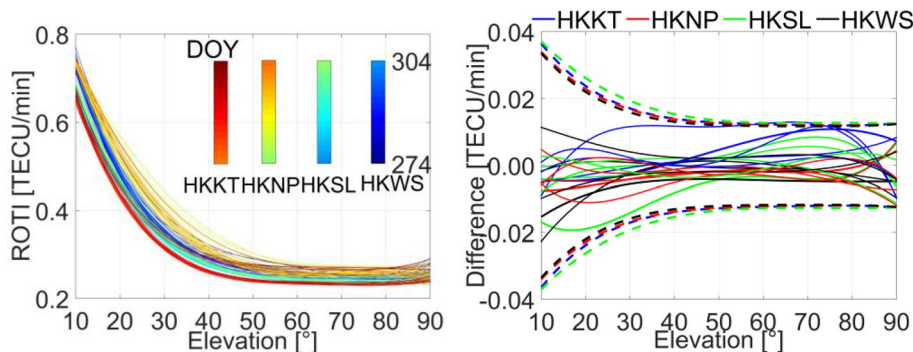


Fig. 10 ROT distribution of HKKT station on DOY 291 (*left*) and 293 (*right*)

$$ROT_k^s \sim N(0, ROTI_k^s) \tag{9}$$

where $N(a, b)$ denotes the Gaussian distribution with mean value a and standard deviation b . Although the ROT distribution on DOY 293 keeps the zero-mean characteristics, a heavy tail is introduced by the scintillation, which cannot be described by the Gaussian distribution. Adjusting the variance of the zero-mean Gaussian distribution can describe a heavy-tailed distribution (Chang 2014; Cheng et al. 2022). Hence, the ROT distribution during the ionospheric scintillation is still formulated as (9) with an adaptive variance determined by ROTI.

Fig. 11 Daily quartic polynomial fitting results of ROTI varying with elevations for four stations in October, presented in different color bars (left), and every difference between the fitting curve on DOY 290 and the fitting curves from DOY 285 to 289 (right). For Fig. 11 (right), the dash lines represent 5% of the fitting curve on DOY 290 for four stations



The conventional elevation-dependent stochastic model is valid for the afore-sunset observations obeying Gaussian distribution in stable ionosphere. As to the post-sunset portion, adaptive factors compensating the elevation-dependent stochastic model are required for mitigating the scintillation impacts. According to (4) and (5), ROTI is mainly interfered by the observation noise and unmodelled errors varying with the satellite elevation. Hence, the daily relationship between elevation and ROTI in stable ionosphere need to be modelled as reference to design the adaptive factors. Notice the aforementioned 30° cutoff elevation is mainly applied for ROTI analysis avoiding the external interferences rather than for kinematic PPP in poor observation condition. To retain the availability of our proposed method in kinematic PPP, 10° cutoff elevation is adopted to the proposed method in the positioning validation. The process of relationship modeling is independent of the afore-sunset real-time PPP.

ROTI before sunset is first classified at every 5° elevation interval. The ROTI mean value of every elevation interval is calculated to extract the modeling coefficients of quartic polynomial fitting model for the relationship between satellite elevation and ROTI as follows

$$\begin{bmatrix} ROTI_{10:15} \\ ROTI_{15:20} \\ \vdots \\ ROTI_{85:90} \end{bmatrix} = \begin{bmatrix} 1 & 12.5 & 12.5^2 & 12.5^3 & 12.5^4 \\ 1 & 17.5 & 17.5^2 & 17.5^3 & 17.5^4 \\ \vdots & \vdots & \vdots & \vdots & \vdots \\ 1 & 87.5 & 87.5^2 & 87.5^3 & 87.5^4 \end{bmatrix} \begin{bmatrix} p_0 \\ p_1 \\ \vdots \\ p_4 \end{bmatrix} \quad (10)$$

where $ROTI_{ele_0:ele_1}$ denotes a vector contains every ROTI value with elevation $ele_0 < E \leq ele_1$. We apply the median number of the elevation interval (e.g., 12.5° for the interval $10^\circ < E \leq 15^\circ$) to represent the interval. $p_0, p_1, p_2, p_3,$ and p_4 are the coefficients of quartic polynomial, reading

$$ROTI_{k,sta}^s = p_4(E_k^s)^4 + p_4(E_k^s)^3 + p_4(E_k^s)^2 + p_4E_k^s + p_0 \quad (11)$$

where $ROTI_{k,sta}^s$ denotes the stable ROTI value at elevation E_k^s . The dense cluster of fitting curves for four stations shows that the polynomial fitting can describe the relationship between elevation and ROTI within a relatively small area (e.g., a city), in Fig. 11 (left). Furthermore, we depict every

difference between the fitting curve on DOY 290 and the fitting curves from DOY 285 to 289, in Fig. 11 (right). The fitting curve divergence can be controlled within 5% in the last 5 days. Thus, when the afore-sunset data is insufficient to conduct a proper fitting, the fitting results within previous 5 days can be valid to the current day.

PPP stochastic model compensation method

After sunset, the epoch-wise fitting ROTI expectation is derived from Eq. (11), while the real-time observed ROTI can be calculated by Eq. (5). The ionospheric random disturbance to the observations can be derived by the difference of two ROT distributions between daily stable ionosphere and real-time ionosphere. In general, Kullback–Leibler divergence (KLD) method is applied to quantify the difference of two distributions, while the empirical KLD formula with the ROT variance portion makes the ionospheric difference increase sharply. It dramatically amplifies the scintillation intensity, which is unconformable to the real observation condition. Hence, we re-formulate the difference of two ROT zero-mean Gaussian distributions as

$$d_k^s = -\log\left(\frac{ROTI_k^s}{ROTI_{k,sta}^s}\right) + \frac{ROTI_k^s}{ROTI_{k,sta}^s} - 1 \quad (12)$$

Equation (12) reaches the minimum value 0 when $ROTI_k^s = ROTI_{k,sta}^s$. Equation (12) is monotonically increasing with $ROTI_k^s > ROTI_{k,sta}^s$, which means the higher ROTI is, the larger d_k^s should be. Hence, d_k^s can effectively present the ionospheric activity. Note that we set $d_k^s = 0, (ROTI_k^s < ROTI_{k,sta}^s)$ in quite real-time ionosphere. Then, a robust factor is designed to compensate the conventional elevation-dependent stochastic model as follows

$$\alpha_k^s = \begin{cases} 1 & d_k^s \leq \theta_1 \\ \exp(d_k^s) - \gamma & \theta_1 < d_k^s \leq \theta_2 \\ \infty & d_k^s > \theta_2 \end{cases} \quad (13)$$

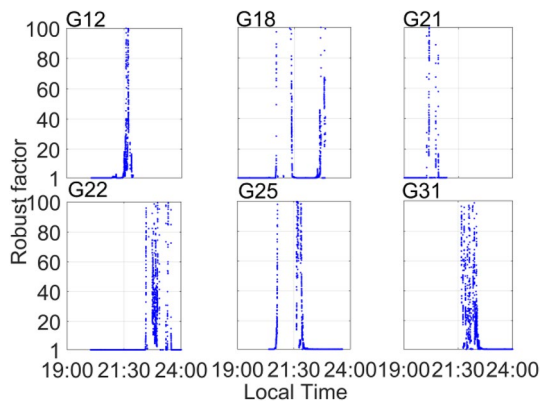


Fig. 12 Robust factors of the scintillation-impacted satellites at HKKT station on DOY 293

where θ_1 and θ_2 are two pre-setting thresholds. θ_1 is calculated from d_k^s between $N(0, ROTI_{k,sta}^s)$ and $N(0, ROTI_{k,sta}^s + \sigma_{ROTI,k}^n)$, where $\sigma_{ROTI,k}$ is the ROTI standard deviation of the n th elevation interval. According to the data analysis of Luo et al. (2022), 99.91% ROTI values scatter within 15TECU/min. θ_2 is calculated from d_k^s between $N(0, 15)$ and $N(0, 0.5)$. To keep the continuity of the robust factor function, γ is designed as $\exp(\theta_1) - 1$. The robust factor tends to be 1 as $ROTI_k^s$ closes to $ROTI_{k,sta}^s$, namely the scintillation intensity decreasing. The proposed piecewise function of the robust factor is adaptive to kinematic PPP in both stable and active ionosphere. The compensated stochastic model reads

$$Q_{com} = \text{blkdiag}(\alpha_k^1 Q_{IF}^1 \cdots \alpha_k^s Q_{IF}^s) \tag{14}$$

where Q_{IF}^s is the elevation-dependent IF stochastic model of the s th satellite. Here, $\text{blkdiag}(\dots)$ denotes a block diagonal matrix.

Figure 12 depicts the robust factors of the scintillation-impacted satellites for HKKT on DOY 293. To correspond with Fig. 2 presenting ROTI series during LT 19:00–24:00, the cutoff elevation is still set to 30° to show the relationship between ROTI and robust factors excluding external interferences. The afore-sunset robust factors are set to 1, while the post-sunset ones ascend with the enlarging ROTI affected by scintillations. The scintillation process is consistent with the irregular’s evolution caused by EPB signatures in Fig. 4. Moreover, the ionosphere during LT 23:00–24:00 seems like stable, leading the robust factors to close to 1. Hence, the proposed compensation method can effectively adjust the elevation-dependent stochastic model in scintillation environment and degrade to the elevation-dependent one in stable ionosphere. Figure 13 further reveals the

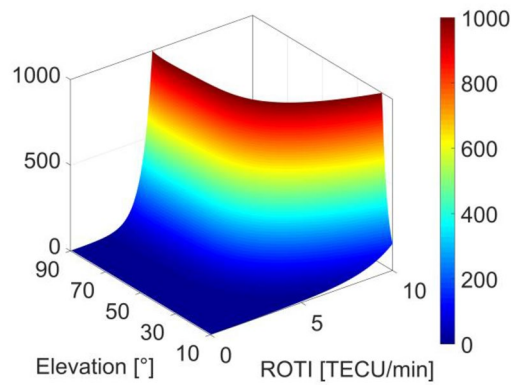


Fig. 13 Relationship between ROTI, elevation, and factor at HKKT on DOY 293

relationship between ROTI and robust factor varying with elevation, where robust factor value (≤ 1000) changes with the color bar.

Experiments and discussions

As analyzed above, the aforementioned dataset is capable to validate the proposed method in stable and active ionosphere for kinematic PPP. The PPP processing strategies and parameter settings are summarized in Table 1. The precise satellite orbit, clock, and DCB products are obtained from IGS products center (<https://igs.org/products/>).

We choose stations HKSL and HKKT on DOY 274 (833 and 874 scintillation epochs), 287 (1872 and 1918 scintillation epochs), 293 (9861 and 10,041 scintillation epochs) and 302 (5632 and 5409 scintillation epochs) for PPP validations in different scintillation environments. The three-dimensional positioning errors of the proposed ROTI and observation precision (ROTI-OP) compensated model, the ROTI and MP (RM)-based model (Li et al. 2022), elevation angle and ROTI stochastic model (EAS-ROTI) (Luo et al. 2022), and conventional elevation-dependent (ED) stochastic model PPP are compared in Fig. 14, respectively. Incorporating with Figs. 3, 7, and 8, dramatic three-dimensional positioning errors of ED scheme are induced by massive abnormalities arising from scintillations after sunset. The maximum position error of ED scheme reaches 23.986 m (DOY 274) and 14.443 m (DOY 302) for HKSL and HKKT stations, while that of ROTI-OP scheme reduces to 0.861 m (DOY 293) and 0.798 m (DOY 293) during four days, respectively. ROTI-OP model has suppressed the error divergence introduced by the scintillation-impacted observations with an adaptive stochastic model compensation. The performance is still deteriorated in the weak observation condition (PDOP 6.84 and 7.38 in maximum for HKKT and HKSL during the scintillation) on DOY 293. Though the RM-based and

Table 1 PPP estimation method

Processing aspects	Settings
Estimation Method	Extended Kalman filtering
Observations	IF pseudorange and phase with GPS L1 and L2
Updating rate	1 Hz
Cutoff elevation	10 °
Ionospheric delay	First-order effect eliminated by IF combination
Troposphere delay	Hydrostatic delays: Saastamoinen model (Saastamoinen 1972) and NMF (Niel 2000, 2001) Wet delays: Estimated with a random walk zenith tropospheric delay parameter
Relativistic effect	Corrected
Sat./Rec. PCO/PCV	Values from igs08.atx
Phase-wind-up	Corrected by the phase polarization effects model (Wu et al. 1993)
Sat. orbit and clock	Values from IGS products
Receiver clock	Estimated as white noise
Ambiguities	Estimated as constant float values

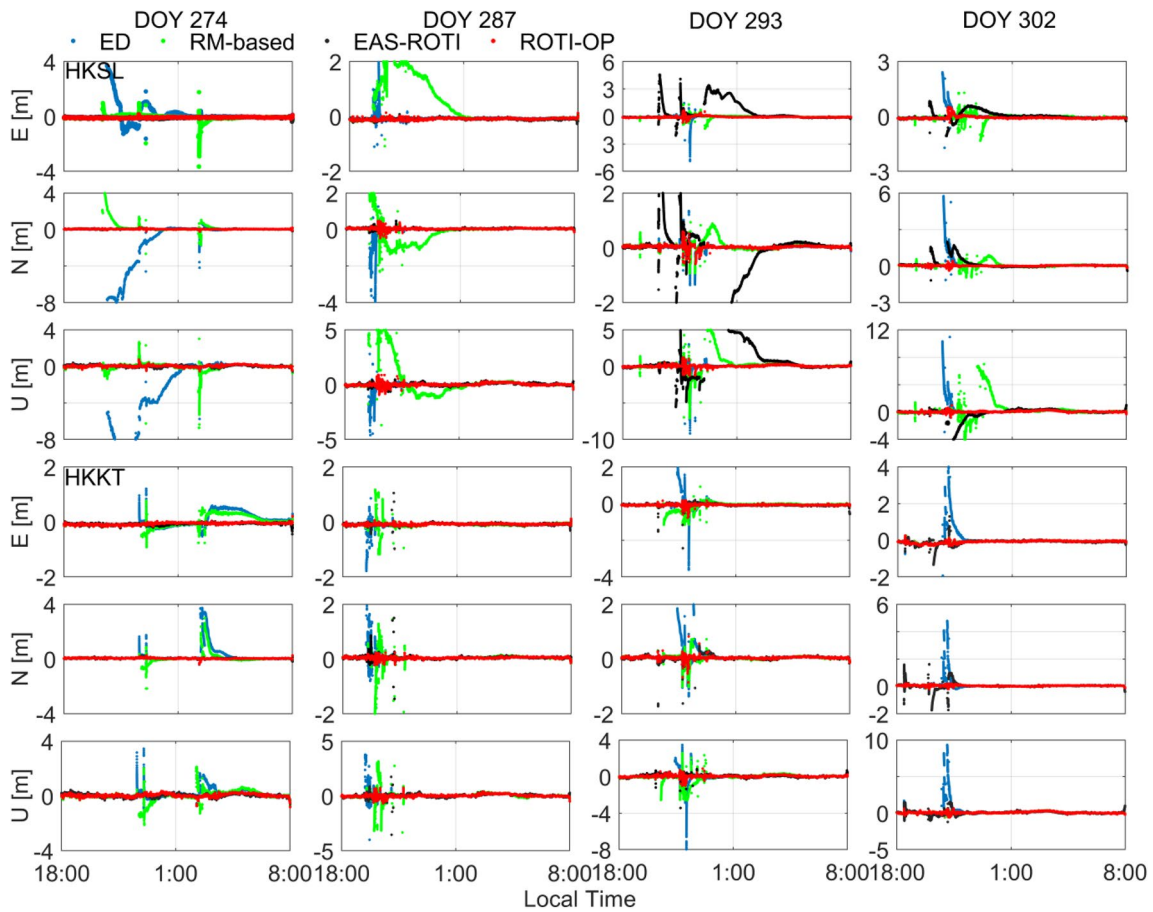
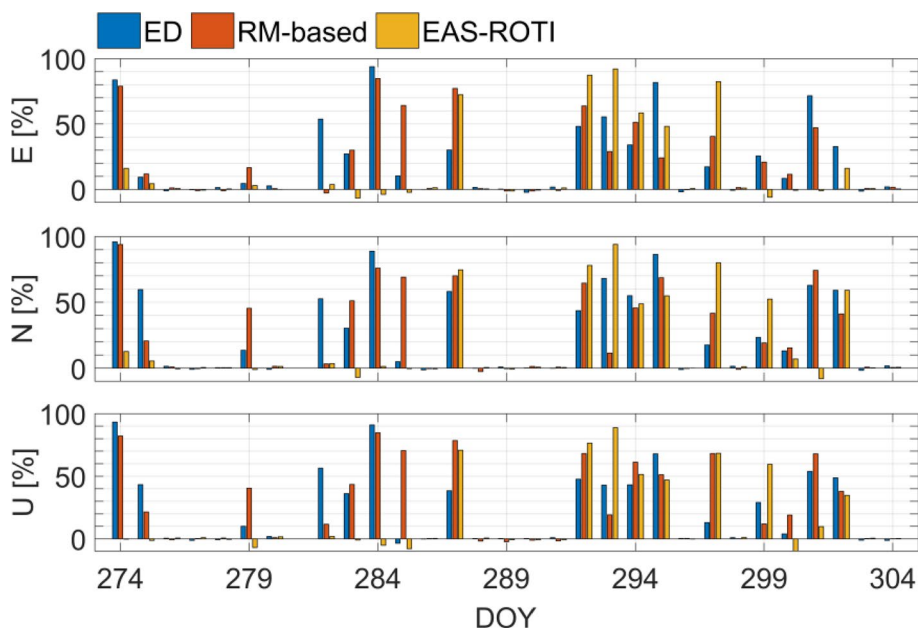


Fig. 14 Three-dimensional positioning errors of ED model (blue), RM-based model (green), EAS-ROTI model (black), and ROTI-OP model (red)

EAS-ROTI performances are similar with ROTI-OP one, they may be deteriorated with the biased compensations of low-elevation scintillation-impacted satellites.

Figure 15 shows the average three-dimensional positioning accuracy improvements of four stations during October for ROTI-OP model, compared with ED model, RM-based

Fig. 15 Average positioning accuracy improvements of four stations in east (*top*), north (*middle*), and up (*bottom*) components for ROTI-OP model compared with ED model, RM-based model, and EAS-ROTI model



model, and EAS-ROTI model. To avoid the scintillation false alarms led by external interferences, the daily scintillation epoch number exceeding 50 is regarded as GNSS signal propagation in active ionosphere, otherwise in stable one. The positioning accuracy improvement of each component is computed as

$$imp_{dir,date}^{mod} = \left[\frac{rms(err_{dir,date}^{ROTI-OP}) - rms(err_{dir,date}^{mod})}{rms(err_{dir,date}^{mod})} \right] \quad (15)$$

where *imp* denotes the improvement; *dir*, *date*, and *mod* denote the direction (including east, north, and up components), the date of observations, and the positioning model (including ROTI-OP, RM-based model, EAS-ROTI, and ED). Here, $rms(err_{dir,date}^{mod})$ denotes the root mean square (RMS) of the positioning error series $err_{dir,date}^{mod}$ from *mod* positioning model in the *dir* component on *date*.

When suffering from the intense scintillations, the ROTI-OP positioning accuracy in east, north, and up components averagely promotes by 43.8%, 52.3%, and 47.8%, compared with ED performance. About 34.7%, 42.0%, and 40.4% average growth are relative to RM-based scheme, and 28.0%, 33.4%, and 27.9% to EAS-ROTI scheme, respectively. Furthermore, the similar PPP performances of four schemes in stable ionosphere demonstrate that ROTI-OP, RM-based, EAS-ROTI models will degrade to ED model as the ionosphere is quiet.

Figure 16 presents the post-sunset three-dimensional positioning error distributions, which demonstrates the superiority of ROTI-OP model attributing to the proper

compensation for low-elevation scintillation-impacted satellites. The horizontal and vertical positioning errors of ROTI-OP model are controlled within 3 m, and those of RM-based model and EAS-ROTI model are within 5 m and 10 m, 6 m and 10 m, respectively. Referring to the dispersion of error distributions, it preliminarily infers that the ionospheric scintillation impairs the positioning solutions more seriously in horizontal than in vertical.

Average RMS of post-sunset three-dimensional positioning errors in October are shown in Table 2. The three-dimensional RMS improvements of ROTI-OP scheme are about 76.2%, 82.2%, and 78.1%, compared with ED scheme. They are 72.4%, 72.0%, and 75.6%, and 63.3%, 60.9%, and 52.3% on average, compared with RM-based scheme and EAS-ROTI scheme.

To further validate the promotion of ROTI-OP model on PPP re-convergence, we simulate 10-min signal outages for every day during the scintillation for HKKT and HKNP from DOY 287 to DOY 293. During the one-week period, DOY 287, 292, 293 suffer from 1918, 13,043, and 10,041 and 1771, 13,522, and 9911 scintillation epochs for HKKT and HKNP stations, which can validate our method in various ionospheric scintillation environments. Note that the outage simulations are set to LT 19:30 to 19:40 from DOY 287 to DOY 291, whereas the outage simulation in DOY 292 and 293 is set to LT 21:30 to 21:40 referring to Fig. 5. Moreover, PPP is regarded as convergence when the three-dimensional positioning errors are continuously lower than 0.5 m for 5 min. As shown in Table 3, the re-convergence performances of ED, RM-based, ROTI-OP models diverse slightly in stable ionosphere, whereas the biased compensations of EAS-ROTI

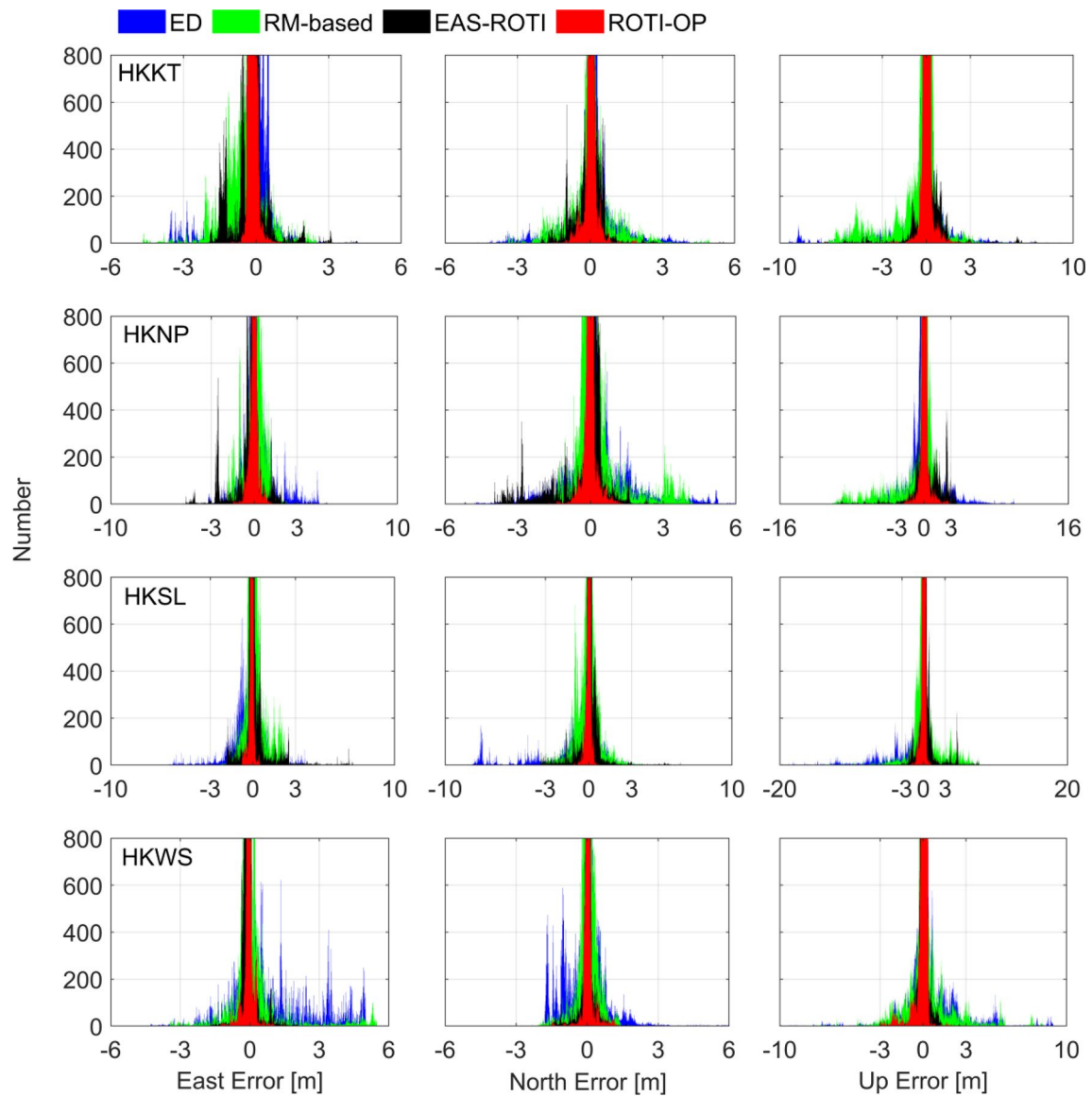


Fig. 16 Post-sunset three-dimensional positioning error distributions of ED model, RM-based model, EAS-ROTl model, and ROTl-OP model for each station in October. Different stations are arranged in different rows (Bar width is 0.01m)

Table 2 Average RMS of post-sunset positioning errors in October

Station	PPP scheme	East [m]	North [m]	Up [m]
HKKT	ED	0.251	0.254	0.538
	RM-based	0.274	0.231	0.520
	EAS-ROTI	0.220	0.159	0.348
	ROTI-OP	0.094	0.068	0.132
HKNP	ED	0.306	0.371	0.625
	RM-based	0.196	0.316	0.648
	EAS-ROTI	0.302	0.281	0.474
	ROTI-OP	0.062	0.051	0.151
HKSL	ED	0.301	0.514	1.145
	RM-based	0.297	0.243	0.761
	EAS-ROTI	0.335	0.255	0.479
	ROTI-OP	0.074	0.045	0.114
HKWS	ED	0.594	0.301	0.697
	RM-based	0.386	0.138	0.593
	EAS-ROTI	0.124	0.085	0.208
	ROTI-OP	0.076	0.066	0.202

model for the low-elevation observations may lead to the worst one. As the ionospheric scintillation happens, the average re-convergence time of ROTI-OP model is reduced by 34.2%, 9.1%, and 31.0% compared with ED model, RM-based model, and EAS-ROTI model, respectively. Hence, ROTI-OP model can evidently mitigate the scintillation impacts on both PPP accuracy and re-convergence time in different ionospheric scintillation environments.

Conclusions

The elevation-dependent stochastic model is severely biased by scintillations. Hence, considering ROTI sensitivity to scintillation detection varying with elevations, we propose a stochastic model compensation method in kinematic PPP. The research findings and conclusions are summarized as follows.

1. Robust factors are constructed to effectively adjust the scintillation-impacted observation precision determined by elevation-dependent model for kinematic PPP.
2. Spatiotemporal stability exists in the daily stable relationship between ROTI and elevation fitted by a quartic polynomial model, suitable for a small area and short-term application scenes (e.g., a city and a few days).
3. Divergence between the fitting and real-time ROT distributions (i.e., in stable and active ionosphere) can describe the scintillation intensity. It is capable to construct robust factors for the scintillation-impacted observations.
4. Numerical comparisons validate the improvement of our method during ionospheric scintillation. The three-dimensional RMS improvements of ROTI-OP scheme are about 76.2%, 82.2%, and 78.1%, compared with ED scheme. They are 72.4%, 72.0%, and 75.6%, and 63.3%, 60.9%, and 52.3%, compared with RM-based and EAS-ROTI schemes. Moreover, average re-convergence time of ROTI-OP model is reduced by 34.2%, 9.1%, and 31.0% compared with ED, RM-based, and EAS-ROTI models, respectively. Moreover, our method degrades to the conventional method in stable ionosphere.

Table 3 Re-convergence time of the different PPP schemes

Station	PPP scheme	Re-convergence time [s]						
		287	288	289	290	291	292	293
HKKT	ED	2188	1431	855	486	844	4262	3856
	RM-based	1038	1423	843	472	850	3950	4376
	EAS-ROTI	1425	1785	2552	1554	2218	4835	4177
	ROTI-OP	1499	1430	855	480	842	1327	3532
HKNP	ED	1572	760	998	826	839	7561	7713
	RM-based	963	803	977	833	835	2882	2551
	EAS-ROTI	1102	1721	2090	1501	1461	7908	3584
	ROTI-OP	1083	761	979	824	835	2654	2338

In summary, the proposed compensation method evidently improves the kinematic PPP performance for both quiet and active ionosphere, especially for various ionospheric scintillation environments.

Acknowledgements This study is sponsored by the National Natural Science Foundation of China (Grant 42204035 and 62073093), the National Key Research and Development Program (Grant 2021YFB3901300), the Science Fund for Distinguished Young Scholars of Heilongjiang Province (Grant JC2018019). All the authors would like to thank Hong Kong Geodetic Survey Services to provide the experimental dataset. We sincerely thank the IGS MGEX campaign for providing multi-GNSS products and the anonymous reviewers for their constructive comments.

Authors' contributions Conceptualization: SC (1) & NZ; Methodology: SC (1) & NZ; Formal analysis and investigation: SC (1), NZ, ZZ; Writing – original draft preparation: SC (1); Writing – review and editing: NZ; Funding acquisition: NZ & JC; Resources: GZ; Supervision: JC; Validation: ZZ; Data curation: SC (6) & GZ; Visualization: SC (6).

Funding National Natural Science Foundation of China (Grant 42204035 and 62073093), the National Key Research and Development Program (Grant 2021YFB3901300), the Science Fund for Distinguished Young Scholars of Heilongjiang Province (Grant JC2018019).

Data Availability The experimental dataset is from Hong Kong Continuously Operating Reference Stations, which is available on <ftp://rinex.geodetic.gov.hk/>. The precise satellite orbit, clock, and DCB products are obtained from international GNSS service (IGS) products center (<https://igs.org/products/>).

Declarations

Competing interests The authors declare no competing interests.

Competing interest We declare that the authors have no competing interests as defined by Springer, or other interests that might be perceived to influence the results and/or discussion reported in this study.

Ethics approval and consent to participate We seriously declare compliance with the ethics standard required by GPS Solutions. This study has no potential conflicts of interest and does not involve human participants and animals.

Consent for publication The authors have read and understood the publishing policy and agree to submit and publish this manuscript in accordance with this policy.

References

- Aquino M, Monico JFG, Dodson AH, Marques H, De Franceschi G, Alfonsi L, Romano V, Andreoti M (2009) Improving the GNSS positioning stochastic model in the presence of ionospheric scintillation. *J Geod* 83(10):953–966
- Barros D, Takahashi H, Wrasse CM, Figueiredo CAO (2018) Characteristics of equatorial plasma bubbles observed by TEC map based on ground-based GNSS receivers over South America. *Ann Geophys* 36(1):91–100
- Blewitt G (1990) An automatic editing algorithm for GPS data. *Geophys Res Lett* 17(3):199–202
- Chang G (2014) Robust Kalman filtering based on Mahalanobis distance as outlier judging criterion. *J Geod* 88(4):391–401
- Cheng S, Cheng J, Zang N, Zhang Z, Chen S (2022) A sequential student's t-based robust Kalman filter for multi-GNSS PPP/INS tightly coupled model in the urban environment. *Remote Sens* 14(22):5878
- Conker RS, El-Arini MB, Hegarty CJ, Hsiao T (2003) Modeling the effects of ionospheric scintillation on GPS/satellite-based augmentation system availability. *Radio Sci* 38(1):1001
- Crane RK (1997) Ionospheric scintillation. In: *Proceedings of the IEEE*, February, 65(2):180–199
- Di Giovanni G, Radicella S (1990) An analytical model of the electron density profile in the ionosphere. *Adv Space Res* 10(11):27–30
- Hernández-Pajares M, Juan J, Sanz J, Orus R, García-Rigo A, Feltnes J, Komjathy A, Schaer S, Krankowski A (2009) The IGS VTEC maps: a reliable source of ionospheric information since 1998. *J Geod* 83(3–4):263–275
- Jacobsen KS (2014) The impact of different sampling rates and calculation time intervals on ROTI values. *J Space Weather Space Clim* 4:A33
- Kelley MC (2009) *The earth's ionosphere: electrodynamic and plasma physics*, 2nd edn. Elsevier, New York
- Kintner PM, Humphreys T, Hinks J (2009) GNSS and ionospheric scintillation. *Inside GNSS* 4(4):22–30
- Klobuchar J (1987) Ionospheric time-delay algorithm for single-frequency GPS users. *IEEE Trans Aero Elec Syst* 3:325–331
- Kouba J, Héroux P (2001) Precise point positioning using IGS orbit and clock products. *GPS Solut* 5(2):12–28
- Leick A, Rapoport L, Tatarnikov D (2015) *GPS satellite surveying*, 4th edn. Wiley, New York
- Luo X, Liu Z, Lou Y, Gu S, Chen B (2017) A study of multi-GNSS ionospheric scintillation and cycle-slip over Hong Kong region for moderate solar flux conditions. *Adv Space Res* 60(5):1039–1053
- Luo X, Lou Y, Gu S, Song W (2019) A strategy to mitigate the ionospheric scintillation effects on BDS precise point positioning: cycle-slip threshold model. *Remote Sens* 11(21):2551
- Luo X, Gu S, Lou Y, Chen B, Song W (2020a) Better thresholds and weights to improve GNSS PPP under ionospheric scintillation activity at low latitudes. *GPS Solut* 24(1):1–12
- Luo X, Gu S, Lou Y, Cai L, Liu Z (2020b) Amplitude scintillation index derived from C/N0 measurements released by common geodetic GNSS receivers operating at 1Hz. *J Geod* 94(2):1–14
- Luo X, Du J, Galera Monico JF, Xiong C, Liu J, Liang X (2022) ROTI-based stochastic model to improve GNSS precise point positioning under severe geomagnetic storm activity. *Space Weather*, 20(7):e2022SW003114
- Li B (2016) Stochastic modeling of triple-frequency BeiDou signals: estimation, assessment and impact analysis. *J Geod* 90:593–610
- Li B, Zang N, Ge H, Shen Y (2019) Single-frequency PPP models: analytical and numerical comparison. *J Geod* 93:2499–2514
- Li C, Hancock CM, Veetil SV, Zhao D, Ham NAS (2022) Mitigating the scintillation effect on GNSS signals using MP and ROTI. *Remote Sens* 14(23):6089
- Liu Z (2011) A new automated cycle slip detection and repair method for a single dual-frequency GPS receiver. *J Geod* 85:171–183
- Moreno B, Radicella S, de Lacy MC, Herraiz M, Rodriguez-Caderot G (2011) On the effects of the ionospheric disturbances on precise point positioning at equatorial latitudes. *GPS Solut* 15(4):381–390
- Ma G, Maruyama T (2006) A super bubble detected by dense GPS network at east Asian longitudes. *Geophys Res Lett* 33(21):L21103
- Morton Y, Yang Z, Breitsch B, Borne H, Xu D, Rino C (2020) Chapter 31: Ionospheric effects, monitoring, and mitigation techniques. In: Morton YJ, van Diggelen F, Spilker JJ, Parkinson B (eds) *Position, navigation, and timing technologies in the 21st Century*. Wiley-IEEE Press, New Jersey

- Niell A (2000) Improved atmospheric mapping functions for VLBI and GPS. *Earth Planets Space* 52(10):699–702
- Niell A (2001) Preliminary evaluation of atmospheric mapping functions on numerical weather models. *Phys Chem Earth (a)* 26(6–8):475–480
- Ott E (1978) Theory of Rayleigh-Taylor bubbles in the equatorial ionosphere. *J Geophys Res Space Phys* 83:2066–2070. <https://doi.org/10.1029/JA083iA05p02066>
- Park J, Veetil SV, Aquino M, Yang L, Cesaroni C (2017) Mitigation of ionospheric effects on GNSS positioning at low latitudes. *Navigation-US* 64(1):67–74
- Pi X, Mannucci AJ, Lindqwister UJ, Ho CM (1997) Monitoring of global ionospheric irregularities using the worldwide GPS network. *Geophys Res Lett* 24(18):2283–2286
- Saastamoinen J (1972) Atmospheric correction for the troposphere and stratosphere in radio ranging of satellites. *Geophysical Monograph* 15. Use of Artificial Satellites for Geodesy. American Geophysical Union, Washington, DC, pp 247–251
- Veetil SV, Aquino M, Marques HA, Moraes A (2020) Mitigation of ionospheric scintillation effects on GNSS precise point positioning (PPP) at low latitudes. *J Geod* 94(2):1–10
- Weng D, Ji S, Chen W, Liu Z (2014) Assessment and mitigation of ionospheric disturbance effects on GPS accuracy and integrity. *J Navig* 67(3):371–384
- Wu J, Wu S, Hajj G, Bertiger W, Lichten S (1993) Effects of antenna orientation on GPS carrier phase. *Manuscr Geod* 18:91–98
- Yang Z, Liu Z (2016) Correlation between ROTI and ionospheric scintillation indices using Hong Kong low-latitude GPS data. *GPS Solut* 20(4):815–824
- Zhang X, Guo F, Zhou P (2014) Improved precise point positioning in the presence of ionospheric scintillation. *GPS Solut* 18(1):51–60
- Zhang Z, Li B, Shen Y, Yang L (2017) A noise analysis method for GNSS signals of a standalone receiver. *Acta Geod Geophys* 52(3):301–316
- Zang N, Li B, Nie L, Shen Y (2019) Inter-system and inter-frequency code biases: simultaneous estimation, daily stability and applications in multi-GNSS single-frequency precise point positioning. *GPS Solut* 24(1):1–13

Publisher's Note Springer Nature remains neutral with regard to jurisdictional claims in published maps and institutional affiliations.

Springer Nature or its licensor (e.g. a society or other partner) holds exclusive rights to this article under a publishing agreement with the author(s) or other rightsholder(s); author self-archiving of the accepted manuscript version of this article is solely governed by the terms of such publishing agreement and applicable law.



Sixiang Cheng is currently a Ph.D. student and received his B.Sc in the College of Intelligent systems Science and Engineering, Harbin Engineering University, China. His research interest is multi-sensor integration in a complicated environment.



Jianhua Cheng is a professor in the College of Intelligent Systems Science and Engineering, Harbin Engineering University, China. His current research activities are related to SINS and integration technology.



Nan Zang obtained her Ph.D. from the College of Surveying and Geo-Informatics, Tongji University, Shanghai, China, and received her B.Sc and M.Sc from the School of Geology Engineering and Geomatics, Chang'an University, China. Her research interests include multi-GNSS precise point positioning and multi-sensors integration in a complicated environment.



Zhetao Zhang Zhetao Zhang obtained his Ph.D. with distinction from Tongji University, where his research topic was the GNSS unmodeled error. He is a researcher at Hohai University. His current research focuses on GNSS precise positioning under complex conditions, including canyon environments, low-cost receivers, and multi-GNSS situations. He was a Postdoctoral Fellow and visiting Ph.D. student at the Hong Kong Polytechnic University and the University of Calgary, respectively.



Guojing Zhao is currently a Ph.D. student in the College of Intelligent Systems Science and Engineering, Harbin Engineering University, China, and received her B.Sc. in the College of Information and Communication Engineering, Harbin Engineering University, China. Her research interest is regional ionospheric modeling and multi-GNSS PPP-RTK in scintillation environment.



Sicheng Chen is currently a Ph.D. student in the College of Intelligent systems Science and Engineering, Harbin Engineering University, China, and received her B.Sc. in the School of Information and Electrical Engineering, Hunan University of Science and Technology, China. Her research interest is resilient multi-sensors integration on indoor and outdoor seamless positioning in urban canyon.